Physics of Fluids

RESEARCH ARTICLE | DECEMBER 28 2023

Drag reduction using riblets downstream of a high Reynolds number inclined forward step flow

Yeteng Wang (王业腾) ; Zhenxu Sun (孙振旭) ; Shengjun Ju (鞠胜军) ; Dilong Guo (郭迪龙); Bo Yin (银波) ; Boyu Pan (潘博宇); Kaiwei Nan (南凯威); Guowei Yang (杨国伟)

Physics of Fluids 35, 125151 (2023)
https://doi.org/10.1063/5.0183742

Physics of Fluids ARTICLE pubs.aip.org/aip/pof

Drag reduction using riblets downstream of a high Reynolds number inclined forward step flow

Cite as: Phys. Fluids **35**, 125151 (2023); doi: 10.1063/5.0183742
Submitted: 24 October 2023 · Accepted: 4 December 2023 ·
Published Online: 28 December 2023

Yeteng Wang (王业腾),[1,2] Zhenxu Sun (孙振旭),[1,a)] Shengjun Ju (鞠胜军),[1] Dilong Guo (郭迪龙),[1] Bo Yin (银波),[1] Boyu Pan (潘博宇),[1,2] Kaiwei Nan (南凯威),[1,2] and Guowei Yang (杨国伟)[1]

AFFILIATIONS

[1]Key Laboratory for Mechanics in Fluid Solid Coupling Systems, Institute of Mechanics, Chinese Academy of Sciences, Beijing, China
[2]University of Chinese Academy of Sciences, UCAS, Beijing, China

[a)]Author to whom correspondence should be addressed: sunzhenxu@imech.ac.cn

ABSTRACT

Micro-riblet is an efficient passive method for controlling turbulent boundary layers, with the potential to reduce frictional drag. In various applications within the transportation industry, flow separation is a prevalent flow phenomenon. However, the precise drag reduction performance of riblets in the presence of flow separation remains unclear. To address this, an inclined forward step model is proposed to investigate the interaction between riblet and upstream flow separation. The large eddy simulation (LES) method is applied to simulate the flow over geometries with different step angles and riblet positions. The results show riblets still reduce wall frictional resistance when subjected to the upstream flow separation. Remarkably, as the angle of the step increases from 0° to 30°, the drag reduction experiences an increment from 9.5% to 12.6%. From a turbulence statistics standpoint, riblets act to suppress the Reynold stress in the near-wall region and dampen ejection motions, thus weakening momentum exchange. Quadrant analysis reveals that with the augmentation of flow separation, the Q2 motion within the flow field intensifies, subsequently enhancing the riblet-induced drag reduction. Moreover, the position of the riblets has a significant impact on the pressure drag. Riblets close to the point of separation enhance flow separation, altering the surface pressure distribution and thus increasing the resistance. The results reveal that when the riblets are positioned approximately 160 riblet heights away from the step, their effect on the upstream flow separation becomes negligible. The precise performance of riblets under complex flow conditions is important for their practical engineering application.

I. INTRODUCTION

Skin-friction drag constitutes a crucial aspect of flow resistance, significantly impacting equipment's energy costs. The development of technologies to reduce friction drag is therefore essential in engineering fluid dynamics design. Notably, microstructures present on the skin of fast-swimming sharks have been identified as effective in reducing flow resistance (Choi *et al.*, 2012). Leveraging this natural inspiration, riblets have been developed, featuring streamwise-aligned surface micro-grooves. These riblets have been considered as a potential passive flow control technology to reduce skin-friction drag. Early pioneering studies obtained a friction drag reduction of up to 8% when the spacing of the riblet was less than 25 wall units, proving the riblet's validity (Walsh, 1982). Bechert *et al.* (1997) investigated the drag characteristics of surfaces with longitudinal riblets and optimized their shape. On a blade riblet surface, they were able to affirm a drag reduction of 9.9%.

The drag reduction mechanism of riblets has also been extensively explored from different perspectives. Based on viscous analyses, Luchini *et al.* (1991) explained the mechanism in Stokes flow. Their explanation is based on the distinction between the protrusion height of cross-flow and that of streamwise flow. Here, the protrusion height referred to the vertical distance between the tip of a riblet and the origin of the Stokes flow. Their analysis suggested that riblets hinder cross-flow, a factor that is considered critical in the turbulence regeneration cycle. Consequently, this hindrance reduces the intermixing of streamwise momentum, leading to a reduction in the frictional drag. Furthermore, the interaction between the riblet and the quasi-streamwise vortices in the turbulent boundary layer is also considered to be the reason for the drag reduction. Lee and Lee (2001) drew the conclusion, supported by particle tracking velocimetry (PTV) measurements, that riblets limit the regeneration of quasi-streamwise vortices. Choi *et al.* (1993) performed direct numerical simulation (DNS) for a channel flow with a riblet surface and reported that the riblet affected ejection and sweep events and inhibited quasi-streamwise vortices in the region near the wall. Goldstein *et al.* (1995) found that

riblets reduce the root mean square (RMS) velocity fluctuations in the vicinity of the riblets by preventing larger turbulence scales from interacting with much of the riblet surface area, resulting in a reduction in high shear stress regions. Additionally, García-Mayoral and Jiménez (2011) claimed that the square root of the riblet cross-sectional area $l_G^+ = \sqrt{A_G^+}$ is a superior descriptor of riblet performance compared to the conventional riblet spacing or depth for arbitrary cross section. profiles. Notably, the optimum l_G^+ was found to be in the range of 9.7–11.7 for different riblet cross section profiles.

Micro-riblet is seen as a promising flow control technology within the realm of the transportation industry, owing to its clear drag reduction mechanism and practical viability. In recent decades, the aerospace industry has maintained a long-standing interest in the technical application of riblets for drag reduction. Viswanath (2002) reviewed the flight test and wind tunnel test in which 3 M riblets were judiciously applied to diverse airfoil configurations, wings, and aircraft structures at a range of velocity regimes and Mach numbers. Kurita *et al.* (2018) investigated the performance of paint riblet in reducing skin friction through flight testing. Zhang *et al.* (2018) employed a large eddy simulation to study the drag reduction of riblet on a low-speed airfoil.

Moreover, the flow control technology of vehicles has been also receiving heightened attention with the development of high-speed trains and new energy vehicles. Aerodynamic frictional drag plays a key role in the overall drag performance of a vehicle. This importance is particularly pronounced in the case of high-speed trains, where frictional drag can account for more than 40% of the total drag. To meet this challenge, micro-riblets offer a promising way of reducing frictional drag in vehicles. However, it is imperative to recognize that the boundary layer on trains and cars is different from that of flat plates or airfoils. The presence of blunt bodies, such as vehicle fronts, leads to flow separation and significant unfavorable pressure gradients, thereby altering the downstream turbulent structures. Few studies have investigated the interaction between pressure gradients and the effectiveness of riblets. It is noteworthy that these studies present incongruent perspectives on the performance of riblets under adverse pressure gradients. Choi (1990) tested riblets in a strong adverse pressure gradient and reported that the skin friction and turbulence conjectures did not change with the pressure gradient. Truong and Pulvin (1989) reported a diminishing efficacy of riblets as adverse pressure gradients intensified. Debisschop and Nieuwstadt (1996) tested trapezoidal riblets in strong adverse pressure and showed almost doubling drag reduction. Klumpp *et al.* (2010) performed large eddy simulations and showed an increase in drag reduction within an adverse pressure gradient. However, Boomsma and Sotiropoulos (2015) compared drag reduction under zero pressure gradient and mild adverse pressure gradient using high-resolution large eddy simulation. They found a consistent drag reduction for riblets regardless of the pressure gradient. In addition, almost all studies focusing on riblet applications to flat plates or two-dimensional airfoils have not considered flow separation effects. Consequently, there are no studies discussing how flow separation affects riblets performance and whether riblets contribute to upstream flow separation. Understanding the behavior of riblets under flow separation conditions is essential for their application in the transportation industry.

To explore the complex interaction between upstream flow separation and riblet-induced drag reduction in turbulent boundary layers, the current study introduces an innovative inclined forward step model with riblets positioned downstream of the step. Gases traversing the forward step at different angles, result in different levels of flow separation. A series of large eddy simulations are applied to calculate the proposed inclined forward step model with different step angles and riblet positions. The remainder of this paper is organized as follows: Section II describes the inclined forward step model and the numerical method. Notably, the numerical method is validated by the DNS data of a channel flow at Reynolds number Re = 2800 from Choi *et al.* (1993). Subsequently, a series of large eddy simulations are performed on the forward step model, encompassing varying inclinations and riblet positions in Sec. III. First, the mechanism behind riblet-induced drag reduction is elucidated. Then, the influence of upstream flow separation on the riblet performance is discussed. Finally, within the same section, the study extends to the impact of riblet positions on the upstream flow separation. Conclusive insights and deductions are summarized in Sec. IV.

II. METHODOLOGY

A. Computational domain and grid configuration

Figure 1 illustrates the geometric configuration of the computational domain. The three primary directions are designated as streamwise (x), vertical (y), and spanwise (z), each associated with the respective velocity components (u, v, and w). The notation superscript "+" signifies quantities scaled by the friction velocity ($u_\tau = \sqrt{\tau_w/\rho}$) and the kinematic viscosity (ν), where τ_w denotes the wall shear stress, and ρ represents the fluid density. The reference length, δ, corresponds to the boundary layer thickness at $x = 10\,\delta$ in the 20° step case without riblets. The spanwise extent of the computational domain is denoted as W, approximately measuring 560 wall units. According to the study of Jiménez and Moin (1991), W is greater than the minimal flow unit inherent to near-wall turbulence. The computational domain's vertical extent at the outlet is defined as $H = 30\delta$. The solid wall can be divided into three sections: the turbulence development section, the inclined forward step section, and the designated working section. The working section is composed of both a flat segment and a riblet segment. The Reynolds number based on the average velocity (U_∞) at the inlet and the length of turbulence development section (L_{dev}) is $Re_L = 5 \times 10^5$. This substantial value ensures the establishment of a fully developed turbulent boundary layer. The angle of the forward step, θ, spans four variations: $\theta = 0°$, 10°, 20°, and 30°. Concerning the working section, the cumulative length of the flat segment, L_{flat}, and riblet segment, L_{riblet}, amounts to 50δ. Notably, L_{flat} is varied in different cases to investigate the effect of the riblet position on the flow structure.

Within the working section, 40 riblets are arranged in a side-by-side configuration along the spanwise direction. The zoom-in drawing of riblet parameters is shown in the top left part of Fig. 1. The spanwise width of each riblet (s^+) measures 14, while the height-over-width ratio ($\frac{h^+}{s^+}$) is fixed to 0.6. The square root of the riblet cross-sectional area ($\sqrt{A_G^+}$) is 10.8, a value aligning with the optimal range as determined by García-Mayoral and Jiménez (2011). They further noted that the optimal geometry configuration is blade type structure, which is adopted in the present research.

At the inlet of the computational domain at $x = -160\,\delta$, the synthetic eddy method (SEM) is employed for the generation of turbulent inflow conditions, which promotes boundary layer transitions. Within

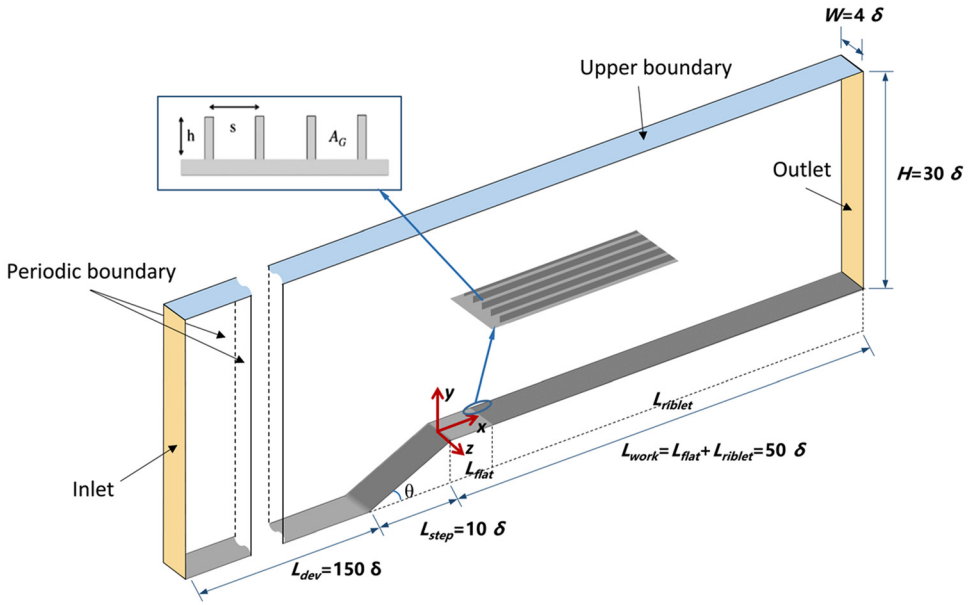

FIG. 1. Sketch of the computational domain with its local enlargement to illustrate the parameters of the riblets geometry.

the SEM framework, the turbulent flow structure is seen as a superposition of spinning eddies. The dimensions of these eddies correspond to the characteristic turbulence scale, which is derived from a preliminary Reynolds-averaged Navier–Stokes (RANS) simulation. Zero pressure outlet conditions are used on the upper and outlet boundary of the domain, while periodic boundary conditions are applied in the spanwise directions. The non-slip conditions are imposed at the wall boundaries, ensuring the adherence of the fluid to the solid surface.

The computational grid has a dimension of $594 \times 800 \times 200$ in streamwise (x), wall-normal (y), and spanwise (z) directions, respectively. In the x direction, the cell size is non-uniformly distributed starting at $\Delta x^+ \approx 14$ near the upper edge of the step and growing to $\Delta x^+ \approx 30$ at the inlet and outlet of the computational domain. Meanwhile, in the z direction, a consistent cell size is maintained, characterized by a resolution of $\Delta z^+ \approx 0.7$. Approximately, 20 nodes per riblet period are used in the spanwise direction to achieve sufficient resolution of the geometry. According to the study of Jelly *et al.* (2014), a spanwise spacing of about one wall unit is sufficient for structured roughness studies. Within the wall-normal (y) direction, the first grid interval is set to be $\Delta y^+_{\text{first}} \approx 0.7$ to capture the small-scale features inherent in turbulence. Gradually, the grid interval scales reach a maximum extent of 60 wall units at the upper boundary. The structural composition and grids of a single riblet segment are visually illustrated in Fig. 2.

B. Numerical algorithm and validation

The governing equations are the unsteady incompressible Navier–Stokes equations, which are discretized by the method of finite volume in CFD simulations. The large eddy simulations (LES) are conducted to solve the equations. The convective flux term is discretized by a bounded central-differencing scheme, which provides a good compromise between accuracy and robustness (Darwish and Moukalled, 1994). For the diffusion terms, a second-order upwind scheme is employed. Meanwhile, to approximate the transient term, the Euler implicit second-order scheme is implemented. A dual time-stepping technique is used to solve the unsteady flow equations, where the internal iteration steps are carefully tuned to ensure that the residuals have a decrease of at least one order of magnitude within each time step. The time step Δt is chosen small enough to ensure that the Courant–Friedrichs–Lewy (CFL) number is generally less than 1. Importantly, the computed time span exceeds 15 flow-through times, symbolized as $(L_{\text{dev}} + L_{step} + L_{\text{flat}} + L_{riblet})/U_\infty$.

The wall-adapting local eddy viscosity (WALE) subgrid scale model (Nicoud and Ducros, 1999) is employed for turbulence closure. This model can provide accurate scaling near walls without using a dynamic procedure. In the near-wall region, the WALE model is recognized for its competence in accurately predicting flow behavior (Ben-Nasr *et al.*,2017; Nicoud and Ducros, 1999; and

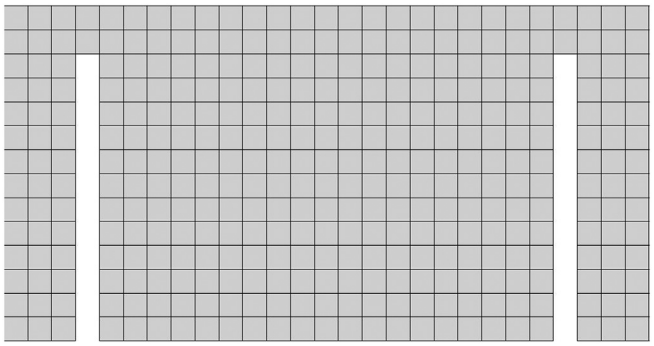

FIG. 2. Riblet segment with grid.

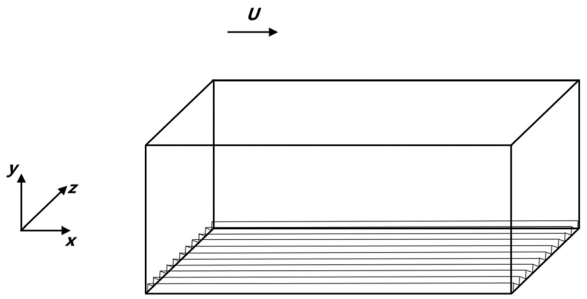

FIG. 3. The computational domain for numerical validation.

Weickert *et al.*, 2010). Validation of the predictive power of the WALE model can be seen in the simulations performed by Temmerman *et al.* (2003) on a channel with hilly topography and periodic constrictions, where the model is compared with direct numerical simulation. In addition, the effectiveness of the WALE model in handling complicated flow problems has been demonstrated, as shown by Jee *et al.* (2016), Medic *et al.* (2016), and Qin *et al.* (2018).

To validate the capability of the numerical method to effectively simulate turbulent boundary layers with riblets, a simulation of a channel flow is conducted. Following the setup outlined by Choi *et al.* (1993), the upper wall is a flat plate, while the lower wall integrates riblets, as shown in Fig. 3. There are 24 riblets with width of $s^+ = 20$ in the computation. The Reynolds number based on the centerline velocity (U_l) of a laminar parabolic profile with the same volume flux and the channel half height (h) is $Re_h = 4200$. The computational domain extends $2\pi \times 2 \times 1.39\,h$ in the streamwise, wall-normal, and spanwise direction. It is resolved by $96 \times 128 \times 360$ grid points. The accuracy of the numerical method is confirmed by the DNS data of Choi *et al.* (1993) and the LES data of Zhang *et al.* (2018). The drag coefficient C_d is defined as follows:

$$C_d = \frac{2F_x}{\rho_0 U^2 S}. \tag{1}$$

Here, the force vector component F_x is computed by integrating all the normal and shear stresses over the objective along the streamwise direction. The reference velocity is U_l, and S is the wetted area of the flat plate. Table I compares the time-averaged drag coefficients from Choi *et al.* (1993) and Zhang *et al.* (2018) and the present study. The results of the present study are very close to the results of the reference DNS and LES data. Comparing the difference of time-averaged drag between the riblet wall and the flat plate, the drag reduction rate is 6.2%, closely aligning with the reference DNS result of 6.4%. Furthermore, Fig. 4 shows the time-averaged velocity profile from the

TABLE I. Drag coefficients for the LES in the present study, the LES from Zhang *et al.* (2018), and the DNS from Choi *et al.* (1993).

	C_d of flat plate	C_d of riblet wall	Drag reduction
Present study	0.003 69	0.003 46	6.2%
Choi *et al.* (1993)	0.003 67	0.003 43	6.4%
Zhang *et al.* (2018)	0.003 70	0.003 44	6.9%

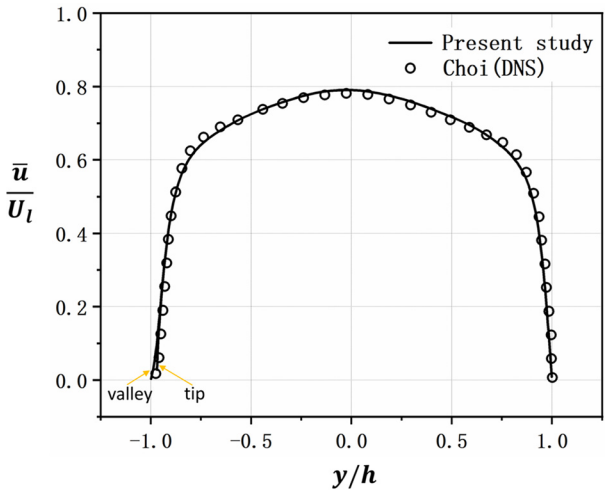

FIG. 4. Time-averaged velocity profile from the riblet to the flat wall in the channel.

riblet to the flat wall. The velocity profiles of the riblet valley and the riblet tip are both presented in the figure. The LES results are in good agreement with the DNS data. Figure 5 compares the velocity normalized by the friction velocity (u_τ) over the flat wall side and the riblet side of the channel. The dashed lines denote the linear and logarithmic $[u^+ = 2.5\ln(y^+) + 5.5]$ segments of the laws of the wall. The profile over the flat wall matches well with the laws. The profile over the tip and valley of the riblet are both presented, where the virtual origin is located at middle between the riblet valley and the riblet tip. There is a slight lift in the logarithmic layer due to the effect of the riblet. These results show that the numerical method is capable of accurately calculating the flow characteristics over the riblets.

III. RESULTS AND DISCUSSION

Having established the simplified geometric model and validating our numerical methodology, our investigation pivots to the intricate interaction between upstream flow separation and downstream riblet-induced drag reduction. This is achieved by systematically varying the

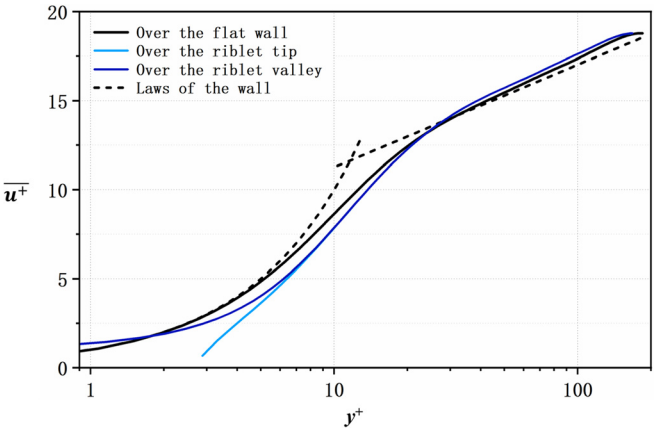

FIG. 5. Variation of mean-velocity profiles normalized by the friction velocity (u_τ).

angle of the step θ and the distance of the riblets from the trailing edge of the step L_{flat}. A comprehensive summary of our simulation permutations is presented in Table II, including the model parameters and results of resistance. The quantification of drag reduction (DR) is expressed through the following equation:

$$DR = \frac{C_{d,clear} - C_{d,riblet}}{C_{d,clear}} \times 100\%, \tag{2}$$

where C_d is the drag coefficient aligned with the streamwise direction, which has been defined in Eq. (1). The subscript "clear" represents the model without riblets, and the subscript "riblet" represents the model with riblets. For the C_d of working section, the reference area S corresponds to the projected area in the wall-normal direction within the streamwise interval $x \in [0, 50\delta]$. For C_d of step, S is defined by the projection of step along the streamwise direction.

A comparison of the drag coefficient (C_d) between the working section of the clear model and that of the riblet model shows that riblets reduce the frictional resistance even when the upstream flow experiences separation. Intriguingly, when the distance (L_{flat}) remains constant, but the step angle (θ) varies across models, the DR of the working section varies. This observation leads to the hypothesis that the performance of riblets is closely linked to upstream flow conditions. There is also an interesting phenomenon where riblets seem to cause an increase in step resistance, which seems to be related to L_{flat}. Section III A takes a comprehensive exploration of these phenomena. First, a detailed analysis of the mechanism underlying the riblet-induced resistance reduction under typical operating conditions is given in Sec. III A. Subsequently, in Sec. III B, we discuss the effect of upstream separation on the downstream performance of riblets. The complex interaction between riblet positioning, pressure distribution, and the drag coefficient (C_d) of the step is examined in Sec. III C.

A. Flow statistics of drag reduction by riblet

This section analyzes the mechanism of riblet-induced drag reduction through a comprehensive investigation involving time-averaged flow field, turbulence statistics, and quadrant analysis. This section, dedicated to the meticulous scrutiny of this mechanism, engenders a comprehensive juxtaposition of flow fields. To this end, a typical case, case 14, characterized by a step angle of 20° and an L_{flat} value of 10δ, is selected. Case 9, which is the clear model without riblet, is used as a control benchmark against case 14. Compared to case 14, the DR of the working section of case 9 is 12.4%, which is higher than that of the flat plate model (case 2). A step angle of 20° is chosen to ensure the occurrence of flow separation. L_{flat} is chosen to be 10δ to exclude the effect of riblet on upstream flow. It is important to note that the subsequent analyses, particularly in Sec. III C, reveal an observation: the proximity of the riblet to the step induces shifts in the intensity of flow separation, which subsequently affects C_d of both the working section and the step. However, the analysis in this section deliberately extricates the influence of riblets on upstream flow separation dynamics. This strategy ensures that the only factor affecting the drag reduction (DR) of the working section remains the interaction between the riblets and the prevailing turbulent structures. The C_d of the step in case 14 is found to be identical to that in case 9, which suggests that the presence of riblets in this case has no discernible effect on the intensity of flow separation. Subsequent analysis can also prove this.

TABLE II. Model parameters and drag coefficients for all simulation cases.

Case	Riblet/clear	Step angle θ	L_{flat} (δ)	C_d of working section	DR of working section	C_d of step
1	Clear	0°	/	0.004 17	/	/
2	Riblet	0°	/	0.003 77	9.5%	/
3	Clear	10°	/	0.004 13	/	0.0595
4	Riblet	10°	0	0.00352	14.9%	0.0670
5	Riblet	10°	2.5	0.003 52	14.9%	0.0617
6	Riblet	10°	5	0.003 60	12.9%	0.0610
7	Riblet	10°	7.5	0.003 69	10.6%	0.0606
8	Riblet	10°	10	0.003 70	10.4%	0.0596
9	Clear	20°	/	0.004 13	/	0.0716
10	Riblet	20°	0	0.003 20	22.5%	0.0857
11	Riblet	20°	2.5	0.003 26	21.1%	0.0745
12	Riblet	20°	5	0.003 51	15.2%	0.0735
13	Riblet	20°	7.5	0.003 59	13.3%	0.0725
14	Riblet	20°	10	0.003 62	12.4%	0.0716
15	Clear	30°	/	0.003 40	/	0.1301
16	Riblet	30°	0	0.002 33	31.4%	0.1438
17	Riblet	30°	2.5	0.002 42	28.8%	0.1326
18	Riblet	30°	5	0.002 73	19.8%	0.1324
19	Riblet	30°	7.5	0.002 87	15.7%	0.1302
20	Riblet	30°	10	0.002 97	12.6%	0.1301

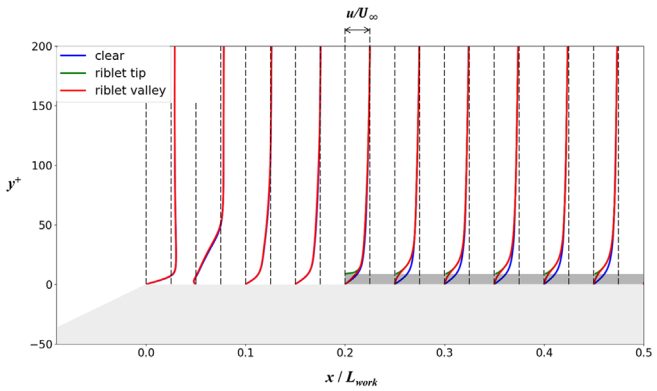

FIG. 6. The evolution of the streamwise velocity profiles in the flow direction of the clear model (case 9) and the model with riblets (case 14).

1. Characteristics of time-averaged flow field

Here, the time-averaged flow field within cases 9 and 14 is discussed. The evolution of streamwise velocity profiles along the flow direction is depicted in Fig. 6. Unlike the flat plate boundary layer, the velocity profile exhibits differences at the riblet tip and riblet valley. Consequently, Fig. 6 presents the velocity profiles over both the riblet tips and valleys. The riblets are positioned between $0.2\,L_{\text{work}}$ and $1.0\,L_{\text{work}}$ in the x direction. The profiles are graphed from 0 to $0.5\,L_{\text{work}}$ in the x direction, with intervals of $0.05\,L_{\text{work}}$. Flow separation occurs at the trailing edge of the forward step, leading to the development of a localized recirculation region around $x/L_{\text{work}} = 0.05$. Between the trailing edge of the step and the riblet region, the velocity profiles of the clear model closely resemble those of the riblet model. This observation suggests that the presence of riblets does not disrupt the upstream flow dynamics within this specific scenario. However, noticeable differences in the velocity profiles become evident over the riblet segment. Specifically, the velocity profiles within the riblet valley exhibit a decelerated flow in comparison with the clear model, with a considerably reduced growth rate near the wall. Meanwhile, growth rates over the riblet tips are slightly larger than those observed in the clear profile. Beyond the immediate vicinity of the riblets, these three velocity profiles converge and experience comparable growth, ultimately reaching the free-stream velocity. It is important to highlight that analogous flow retardation and mean velocity profiles have been previously documented in the context of flat plate flow with riblets (El-Samni *et al.*, 2007; Goldstein *et al.*, 1995).

The exploration of streamwise vortices is important in understanding the interaction between the riblet and the three-dimensional flow in turbulent boundary layers. Within the time-averaged flow fields, it has been established that riblet surfaces induce counter-rotating streamwise vortices, a phenomenon well documented in prior research. Here, the time-averaged streamwise vorticity within case 14 is discussed. The streamwise vorticity is defined as

$$\omega_x = \frac{\partial v}{\partial z} - \frac{\partial w}{\partial y}. \tag{3}$$

Figure 7 presents contour plots illustrating the distribution of time-averaged ω_x in proximity to the riblets at planes corresponding to $x/L_{\text{work}} = 0.3,\ 0.5,\ 0.7,$ and 0.9. Notably, these contours show

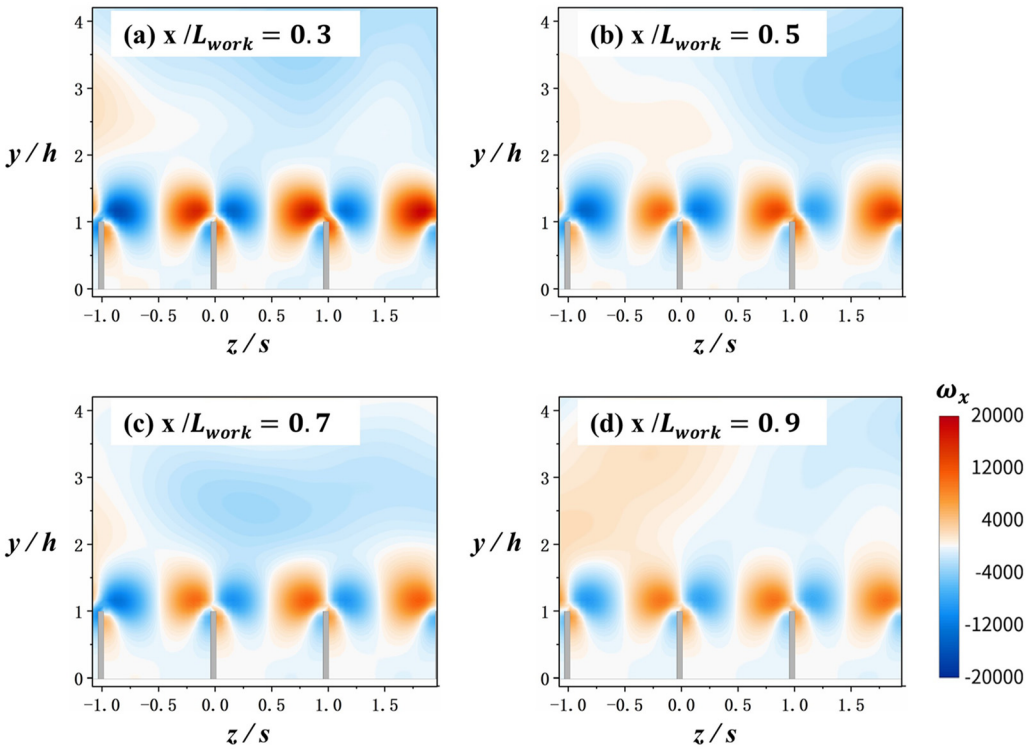

FIG. 7. Time-averaged streamwise vorticity contours near riblet surface of case 14, at planes of $x/L_{\text{work}} = 0.3,\ 0.5,\ 0.7,$ and 0.9.

rotating vortex tubes near the riblet tips, with a diameter approximately half width of the riblet. In addition, there are regions of high vorticity on both sides of the riblet tips. As the x-coordinate progresses, the maximum magnitude of the streamwise vorticity decreases. A similar trend was reported by Raayai-Ardakani and McKinley (2019), who studied micro-riblets in laminar flows at high Reynolds numbers.

2. Turbulence statistics

To elucidate the underlying physical mechanisms for riblet-induced drag reduction, turbulence statistics from the turbulent flow at several streamwise positions are presented. Figure 8 illustrates the streamwise components of the normal Reynolds stress ($\overline{u'u'}$) vs wall distance y^+ at locations corresponding to $x/L_{\text{work}} = 0.3,\ 0.5,\ 0.7,$ and 0.9. For the turbulence statistics over riblets in the present study, the virtual origin is located at the riblet valley. Significant variations of the normal Reynold stress are observed within the inner region of the turbulent boundary layer. The plot clearly indicates that in the proximity of the riblets, both within and beyond the riblet valleys, the Reynolds stress is attenuated. The peak of the normal stress is situated within the buffer layer, and at each of the mentioned positions, the peak value in the riblet model is lower than that in the clear model. As the distance from the wall increases, the profile of normal Reynolds stress in the riblet model aligns with the profile in the clear model within the logarithmic layer. The attenuation of normal Reynold stress serves as evidence that riblets can effectively suppress the turbulence intensity near the wall, which is consistent with the study on flat plate equipped with riblets (Boomsma and Sotiropoulos, 2015; Choi *et al.*, 1993). The peak values of normal stress and the suppression of normal stress by the riblet are different at different streamwise positions, which may be attributed to the influence of upstream flow separation on the turbulence structures of the boundary layer.

In high Reynolds number flows, the wall frictional resistance exhibits a strong correlation with the Reynolds shear stress. This correlation can be exemplified through the case of a flat plate flow. In the context of turbulent flow within a channel bounded by two infinite parallel flat plates under the influence of a constant pressure gradient, the streamwise mean motion equation yields the following expression:

$$\mu\frac{dU}{dy} - \rho\langle u'v'\rangle = \tau_\omega\left(1 - \frac{y}{\delta}\right), \tag{4}$$

where y represents the vertical direction, δ is the half height of the channel, and τ_ω denotes the wall shear stress. The wall friction coefficient is defined as $C_f = \tau_\omega/\left(\rho U_{AVG}^2\right)$, where U_{AVG}^2 stands for the average velocity of the cross section. C_f can be obtained by integrating Eq. (4),

$$C_f = \frac{3}{Re_{AVG}} - \frac{3}{\delta^2 U_{AVG}^2}\int_0^\delta (\delta - y)\langle u'v'\rangle dy, \tag{5}$$

where $Re_{AVG} = U_{AVG}\delta/\upsilon$. The first term on the right-hand side of the above-mentioned equation is related to viscosity and corresponds to the wall friction coefficient for laminar flow. The second term represents the integral of the Reynolds shear stress, which stands for the main contributor to wall friction in highly turbulent flows. Comparison of the Reynolds shear stress distribution helps to comprehend the mechanism of riblet-induced drag reduction. Figure 9 illustrates the variation of Reynolds shear stress ($\overline{u'v'}$) against wall distance at several streamwise positions. The variations in the shear stress caused by the riblets are similar to those observed in normal stress. Apparently, the Reynolds shear stress is attenuated in proximity to the riblet. Moreover, the peak Reynolds shear stress of the riblet model is significantly lower than that in the clear model. This observation indicates that the process of momentum transportation is suppressed by the riblet.

3. Quadrant analysis of Reynolds shear stress

An in-depth analysis of momentum transport and the generation of turbulent kinetic energy within the near-wall region can be achieved through quadrant analysis of Reynolds shear stress. The signs of the streamwise velocity fluctuations (u') and the wall-normal velocity fluctuations (v') are recognized to contain useful information of boundary layer flow. Velocity fluctuations are categorized into four distinctive groups: Q1 ($+u'$, $+v'$), Q2 ($-u'$, $+v'$), Q3 ($-u'$, $-v'$), and Q4 ($+u'$, $-v'$), which were called the quadrants of the Reynolds shear stress plane (Wallace, 2016). It is worth noting that Q2 and Q4 are gradient-type motions, which are clearly related to the ejection and sweep events in the near-wall region, respectively. The term gradient-type motion is

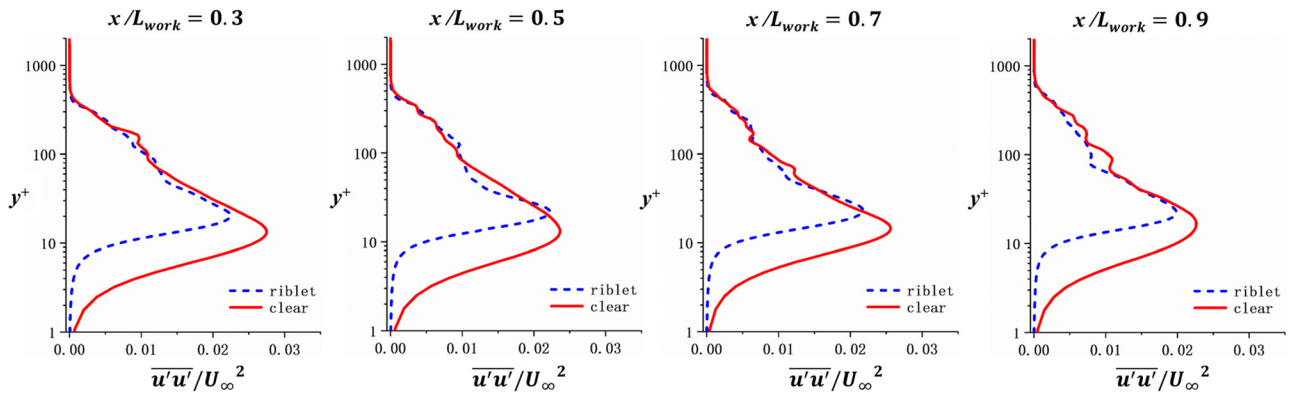

FIG. 8. The profile of the streamwise components of the non-dimensional normal Reynolds stress $\overline{u'u'}/U_\infty{}^2$ at streamwise positions of $x/L_{work} = 0.3,\ 0.5,\ 0.7,\ 0.9$.

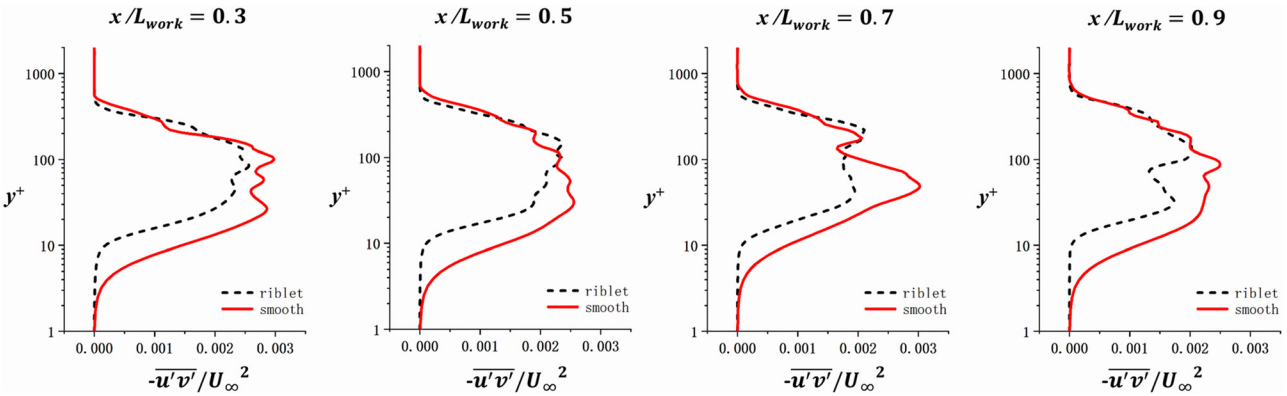

FIG. 9. The profile of the non-dimensional Reynolds shear stress $-\overline{u'v'}/U_\infty{}^2$ at streamwise positions of $x/L_{\text{work}} = 0.3,\ 0.5,\ 0.7,$ and 0.9.

used to indicate vertical momentum fluxes due to fluid elements moving up and down having a streamwise momentum that is less or greater than the local mean streamwise momentum, respectively. It is often assumed that Q2 and Q4 motions make the largest contributions to the Reynolds shear stress, whereas the Q1 and Q3 motions signify outward and inward interactions.

A thorough investigation into the primary physical processes contributing to the attenuation in the Reynolds shear stress induced by riblets is conducted through quadrant analysis. Figure 10 shows the distribution of the motions across the four quadrants at the height of $y^+ = 30$. Evidently, the peak of each quadrant is located at approximately 0.05 L_{work}, which aligns with the center of the separation region following the step. Focusing specifically on the region over the riblet [0.2 L_{work}, 1.0 L_{work}], Q2 and Q4 contribute considerably more to the turbulent shear stress than Q1 and Q3. Q1 and Q3 are small and nearly identical for both the clear model and the flat plate. As can be seen, Q2 decreases significantly over the riblet, while Q4 shows no obvious change. Consequently, the ejection motions in turbulence boundary layer are effectively suppressed by the presence of riblets, which emerge as the primary factor behind the reduction in the Reynolds shear stress. Ejection motions, characterized by the expulsion of near-wall fluid, account for much of the outward vertical transport of momentum and thus for the high frictional resistance in turbulent flow.

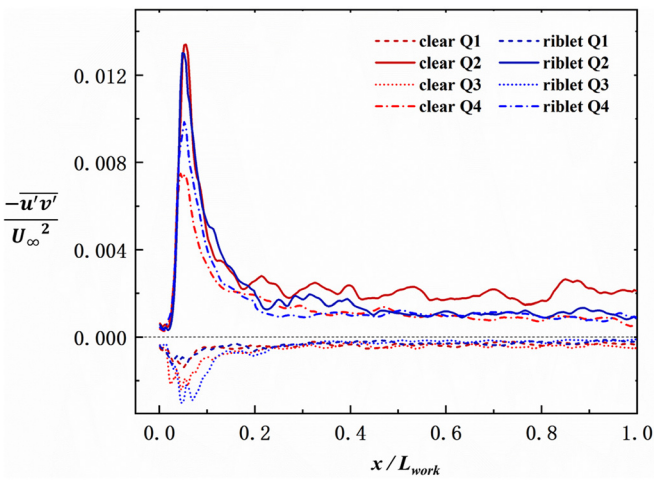

FIG. 10. The quadrant analysis of Reynolds shear stress for the clear model and the riblet model at $y^+ = 30$.

B. Influence of separation on downstream riblets performance

Table II reveals distinct variations in the drag reduction (DR) of the working section among models featuring different step angles (θ) but a consistent L_{flat}. Therefore, the performance of riblets is influenced by the strength of the upstream separation. This section analyzes cases 2, 8, 14, and 20, where the step angles are 0°, 10°, 20°, and 30°, respectively, while maintaining $L_{flat} = 10\delta$. Additionally, for comparative purposes without riblets, cases 1, 3, 9, and 15 are studied correspondingly. The reason for choosing the model with $L_{\text{flat}} = 10\delta$ is the same as in Sec. III A. This choice ensures that riblet performance is the sole factor impacting the drag reduction within the working section.

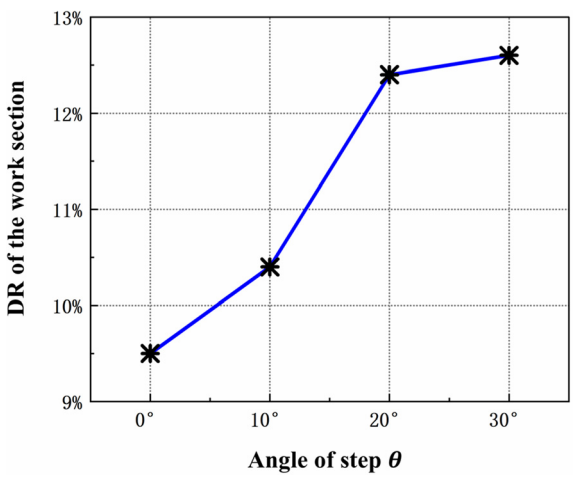

FIG. 11. The DR of the working section varies with the angle of step θ.

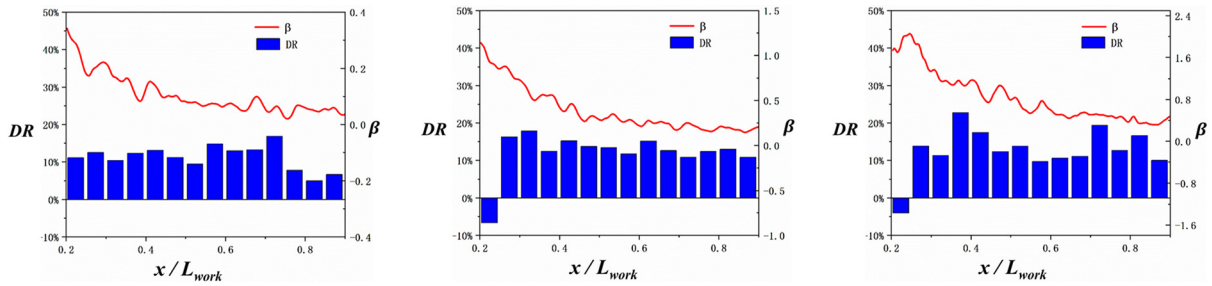

FIG. 12. Distribution of pressure gradient along the flow direction and *DR* of individual segments from 0.2 L_{work} to 0.9 L_{work}: (a) 10° step angle case; (b) 20° step angle case; and (c) 30° step angle case.

Figure 11 illustrates the *DR* of the working section for cases with different step angles. Notably, as the step angle increases, the *DR* increases from 9.5% to 12.6%. This rise in *DR* is linked to the augmentation of flow separation caused by larger step angles. Such augmentation leads to downstream changes, primarily in pressure gradient intensity and flow structures. The underlying causes for the amplified *DR* linked to increased step angles are analyzed below in terms of these two changes.

The Clauser parameter (β) characterizes the pressure gradient and is defined by the following equation:

$$\beta = \frac{\Delta^*}{\tau_w}\frac{\mathrm{d}p}{\mathrm{d}x}, \tag{6}$$

where Δ^* represents the displacement thickness, τ_w is the wall shear stress, and $\mathrm{d}p/\mathrm{d}x$ is the pressure gradient in the direction of flow. To explore the interaction between the pressure gradient and riblets performance, we uniformly divided the wall from $x/L_{\mathrm{work}} = 0.2$ to $x/L_{\mathrm{work}} = 0.9$ into 14 segments. For each segment, the drag coefficients (C_d) and drag reduction (*DR*) is counted individually. The distributions of pressure gradient and the *DR* for each segment are shown as the Fig. 12. Upon comparing Figs. 12(a)–12(c), it can be seen that as the step angle increases from 10° to 30°, the overall Clauser parameter also experiences a corresponding rise. This shift is consistent with the change in *DR* of the working section. However, looking at the pressure gradient within just one case reveals that it also varies significantly along the flow direction. For example, in the case of a 20° step, the pressure gradient gradually decreases from strong ($\beta > 1$) to mild ($\beta < 0.25$) along the flow direction. Nonetheless, there is no significant tendency for the *DR* to increase or decrease in the individual segments. Similarly, in the other two cases, no direct correlation is found between segment drag reduction and pressure gradient. Although an augmented adverse pressure gradient may coincide with an elevated *DR* overall, the connection between local riblet-induced drag reduction and pressure gradient strength remains indistinct.

Section III A highlights the influence of riblets on the turbulence structure by suppressing ejection motions, which can be represented by the Q2 quadrant of Reynolds shear stress. Consequently, the distributions of the Q2 quadrant motions along the flow direction at $y^+ = 30$ in cases with different step angles are shown in Fig. 13. Evidently, a higher Q2 motion emerges in the near-wall region following passage through a step with a large angle. This augmentation in ejection motions within the boundary layer is attributed to the stronger flow separation upstream. The wake flows resulting from separation may influence both turbulence intensity and structure within the boundary layer. Moreover, riblets exhibit more pronounced Q2 suppression in the case with a larger step angle.

To quantify the Q2 alterations, Table III counts the mean value of Q2 at $y^+ = 30$, the Q2 proportion within the shear stress, and the Q2 reduction attributed to riblets. Q2 proportion is the percentage of components with negative streamwise velocity fluctuations and positive wall-normal velocity fluctuations at the same time in the Reynolds shear stress integration process. Q2 reduction is the ratio of reduction in the mean value of Q2 for the riblet model compared to the smooth model with the same step angle. As the step angle increases, not only does the mean value of Q2 rise, but the proportion of Q2 within Reynolds stress also increases. Correspondingly, the Q2 reduction achieved by riblets improved from 23.7% to 43.8%. This variation in Q2 elucidates the rationale behind the *DR* enhancement associated with increasing step angles.

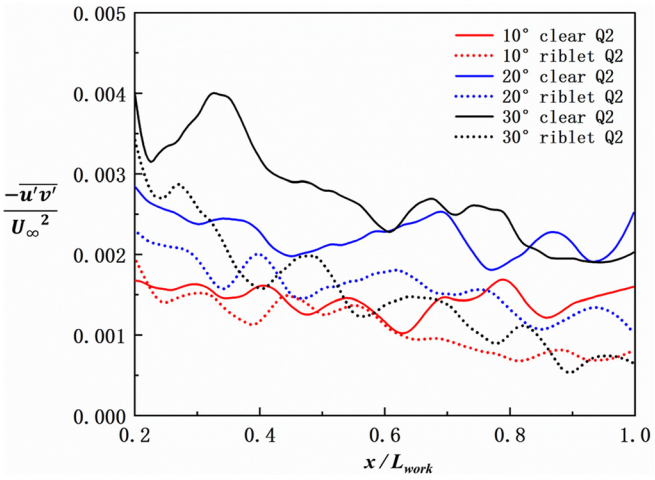

FIG. 13. The Q2 quadrant of Reynolds shear stress for the cases with different step angles at $y^+ = 30$.

TABLE III. Mean values of Q2 for the cases with different step angles at $y^+ = 30$.

Case	Riblet/clear	Step angle θ	*DR* of working section	Mean value of Q2	Q2/Reynolds shear stress	Reduction of Q2
3	Clear	10°	/	0.001 44	72.2%	/
8	Riblet	10°	10.4%	0.001 10	71.6%	23.7%
9	Clear	20°	/	0.002 05	88.1%	/
14	Riblet	20°	12.4%	0.001 23	71.1%	39.9%
15	Clear	30°	/	0.002 71	98.9%	/
20	Riblet	30°	12.6%	0.001 52	78.9%	43.8%

C. Effect of riblets position on pressure distribution and pressure drag

As well as reducing frictional resistance, the riblets can also affect the distribution of pressure, altering the pressure drag of the forward step. Table II highlights that the position of riblets is the primary factor in determining the pressure distribution. To explain in detail the effect of the riblet position, the flow fields of cases 10, 11, 12, and 14 are analyzed in this section. These cases entail L_{flat} value of 0δ, 2.5δ, 5δ, and 10δ, respectively, all featuring a step angle of 20°. Case 9 without riblet is the corresponding simulation for comparison. Figure 14 presents the drag coefficient (C_d) of the step across cases with varying L_{flat}. Notably, when the riblet is positioned immediately behind the step, the drag of the step is maximized, increasing by 19.7% compared to the clear model. With an increase in L_{flat}, the drag of the step decreases. Until reaching $L_{flat} = 10\delta$, the drag of the step aligns with that observed in the clear mode.

Figure 15 illustrates the distribution of time-averaged pressure on both the step and the working section. At the leading edge of the step, a positive pressure zone emerges due to the flow's deceleration, while the flow accelerates and separation occurs near the trailing edge of the step, resulting in a pronounced negative pressure zone. Comparing Figs. 15(a) and 15(b), the riblet positioned to the step significantly weakens the negative pressure zone, resulting in increased pressure drag on the step. This phenomenon is not evident after $L_{flat} > 2.5\delta$. For a quantitative evaluation of the influence of riblets position on pressure distribution, Fig. 16 illustrates the pressure distribution along the flow direction on the centerline of the step. The model with $L_{flat} = 0$ exhibits overall higher surface pressure compared to the clear model. Specifically, the pressure is elevated by 400 Pa near the trailing edge of the step. Models with $L_{flat} = 2.5\delta$, 5δ, 10δ display pressure profiles similar to the clear model. The locally enlarged graphs reveal slight pressure increase near the trailing edge of the step for models with $L_{flat} = 2.5\delta$, 5δ. Differences in surface pressure distribution align cohesively with variations in the pressure drag of the step.

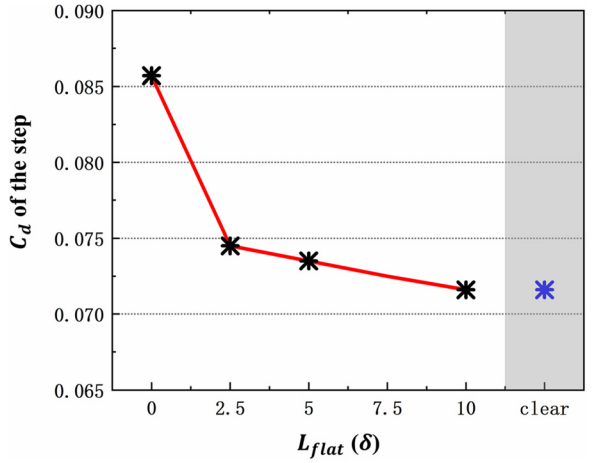

FIG. 14. The drag coefficient C_d of step varies with the L_{flat}.

The time-averaged streamlines colored with velocity values at the midplane for both the case without riblet and cases with varying L_{flat} are shown in Fig. 17. In all cases, flow separation is observed from the trailing edge of the step. A flow separation bubble appears in the separated shear layer, and the separated flow reattaches to the working section downstream. In the case with L_{flat} of 0, the region of flow separation is the largest. As L_{flat} increases, the flow separation region decreases, and the flow separation region becomes as large as that of the clear model when $L_{flat} = 10\delta$. The reattachment length (R) is defined as the distance between the flow separation point and the reattachment point to quantify the size of the flow separation region (Akbarzadeh and Borazjani, 2019; Mueller and DeLaurier, 2003). The reattachment lengths for these cases are listed in Table IV. The R value for the case with L_{flat} of 0 is $4.84\,\delta$, signifying a 64.6% increase compared to the clear model. This enhanced flow separation can potentially be attributed to the presence of riblets close to the step, disturbing high-velocity fluid and augmenting flow instability. The increased flow separation in turn leads to reduced flow velocity at the trailing edge of the step, culminating in increased pressure on the step. In addition, similar phenomena occur for models with other step angles. Considering that the separation bubbles of models with a 10° step are not significant, the reattachment length (R) of models with a 30° step has been counted, as shown in Table V. It also indicates that the smaller L_{flat} the more R increases, and the value of R shows a clear positive correlation with the drag of the step. Both Tables IV and V show that the reattachment length and the drag coefficients of step for $L_{flat} = 10\delta$ are consistent with the model without the riblet. This indicates a critical length whose effect on flow separation is negligible once the distance between the groove and the separation point is greater than the critical length. This indicates the existence of a critical length, which determines whether the effect of the riblet on flow separation can be neglected. Considering that the effect of the riblet on the flow separation could be related to the perturbation of the flow by the shape of the projection, it is proposed to characterize this critical length by the height of the riblet. The critical length is approximately 160 riblet heights, which applies to the models with the step of 10°, 20°, and 30°

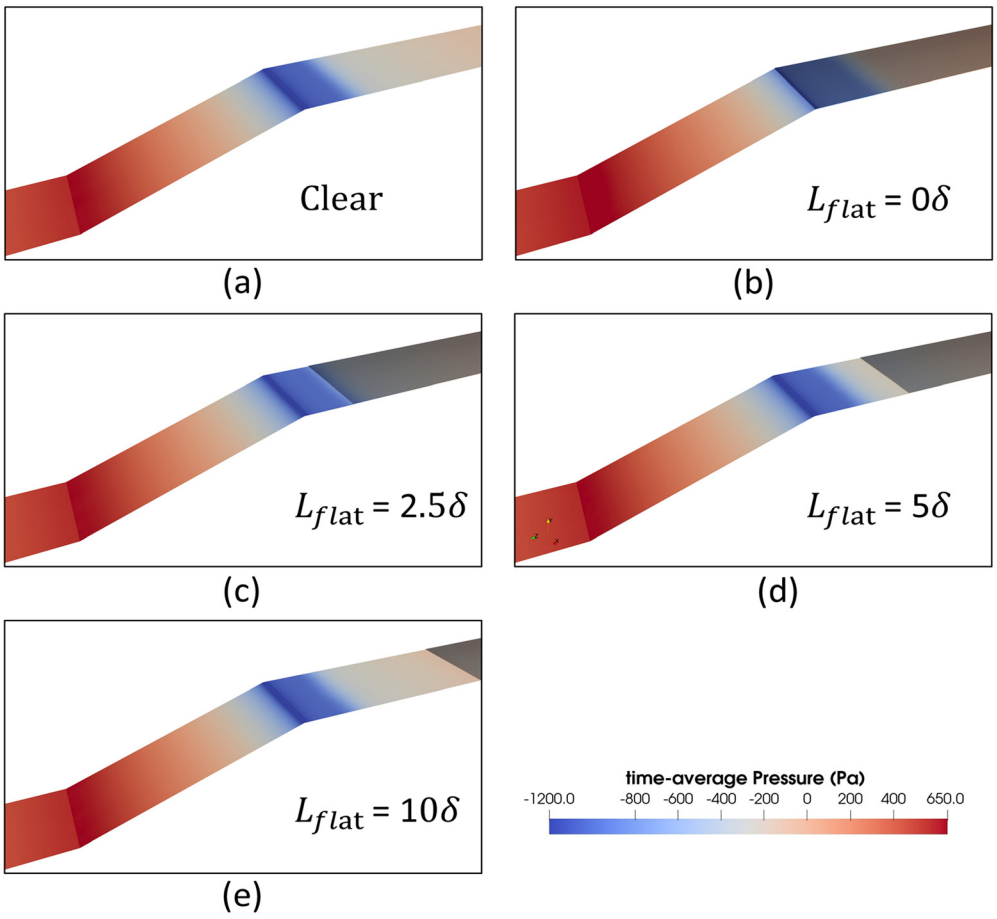

FIG. 15. Contours of the time-averaged pressure on the step and the working section: (a) case without riblet; (b) case with L_{flat} of 0; (c) case with L_{flat} of 2.5 δ; (d) case with L_{flat} of 5 δ; and (e) case with L_{flat} of 10 δ.

in the present study. Increased resistance from improperly installed riblets is unfavorable in engineering applications and needs to be mitigated. It could be a valuable reference that the riblet should be more than 160 riblet heights away from the separation point.

IV. CONCLUSIONS

In this study, an inclined forward step model is proposed to investigate the interaction between riblet-induced drag reduction and upstream flow separation. Using large eddy simulation techniques, the flow was calculated in various scenarios with different step angles and riblet positions. The present study uncovers the principles of riblet behavior in flows with separation, contributing to the wider application of riblets in complex flow scenarios, such as high-speed vehicles. The interaction between riblet-induced drag reduction and upstream flow separation can be summarized as the following key insights:

(1) Riblets still reduce wall frictional resistance when subjected to the upstream flow separation. By studying the time-averaged flow field and the turbulence statistics, it is found that riblets could suppress Reynolds stress in the near-wall region. Furthermore, the deeper reason for the reduction in the Reynolds shear stress is investigated by quadrant analysis. The ejection motions, represented by Q2, in the turbulent boundary layer, are suppressed through riblet influence.

(2) Riblets exhibit enhanced drag reduction efficacy under the influence of upstream flow separation. While ensuring the riblets do not affect the upstream flow separation, drag reduction increases from 9.5% to 12.6% as the step angle increases from 0° to 30°. By analyzing the resistance of the segments, it is concluded that the pressure gradient may not be the primary determinant behind the drag reduction variation. Quadrant analysis shows that with augmented flow separation, Q2 motion in the flow field increases, consequently elevating riblets' drag reduction capability.

(3) The pressure drag increases when the riblet is close to the separation point. Riblets located near the separation point promote flow separation and diminish local flow velocity. This cascade effect results in increased pressure on the step, increasing pressure drag. This increment in pressure drag should be avoided in practical engineering applications. The results of models with different step angles indicate the existence of a critical length, which determines whether the effect of the riblet on flow

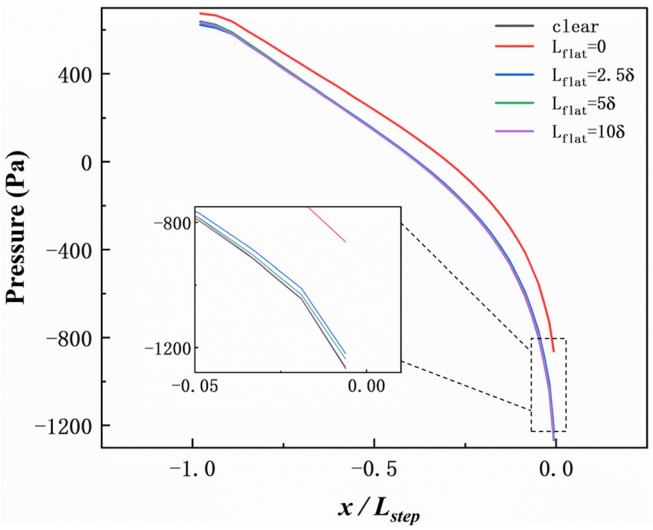

FIG. 16. Distribution of time-averaged pressure on the centerline of the forward steps.

separation can be neglected. The present study favors the non-dimensional riblet position x/h to characterize the critical length, which is approximately 160 riblet heights.

The excellent drag reduction performance of the riblet in high Reynolds number flows with separation provides a basis for application on flight with large angles of attack and ground carriers such as vehicles. Meanwhile, the relationship between the riblet location on the flow separation strength can guide the installation of the riblet on vehicles. However, limited by computational resources, the present study could not adequately reflect the micro-riblet in real vehicles, because the curved surface of the vehicle is more complex and the flow around the body has three-dimensional effects. The uncertainty of the incoming flow conditions during operation is also an important challenge in applying riblets on vehicles. In the future, we may model the performance of the riblet to reduce the cost of numerical simulation

TABLE IV. Reattachment length R for the 20° models with different L_{flat}.

Case	Riblet/ clear	Step angle θ	L_{flat} (δ)	C_d of step	Reattachment length R (δ)
9	Clear	20°	/	0.0716	2.94
10	Riblet	20°	0	0.0857	4.84
11	Riblet	20°	2.5	0.0745	3.85
12	Riblet	20°	5	0.0735	3.00
14	Riblet	20°	10	0.0716	2.95

TABLE V. Reattachment length R for the 30° models with different L_{flat}.

Case	Riblet/ clear	Step angle θ	L_{flat} (δ)	C_d of step	Reattachment length R (δ)
15	Clear	30°	/	0.1301	4.75
16	Riblet	30°	0	0.1438	6.82
17	Riblet	30°	2.5	0.1326	5.48
18	Riblet	30°	5	0.1324	5.12
20	Riblet	30°	10	0.1301	4.73

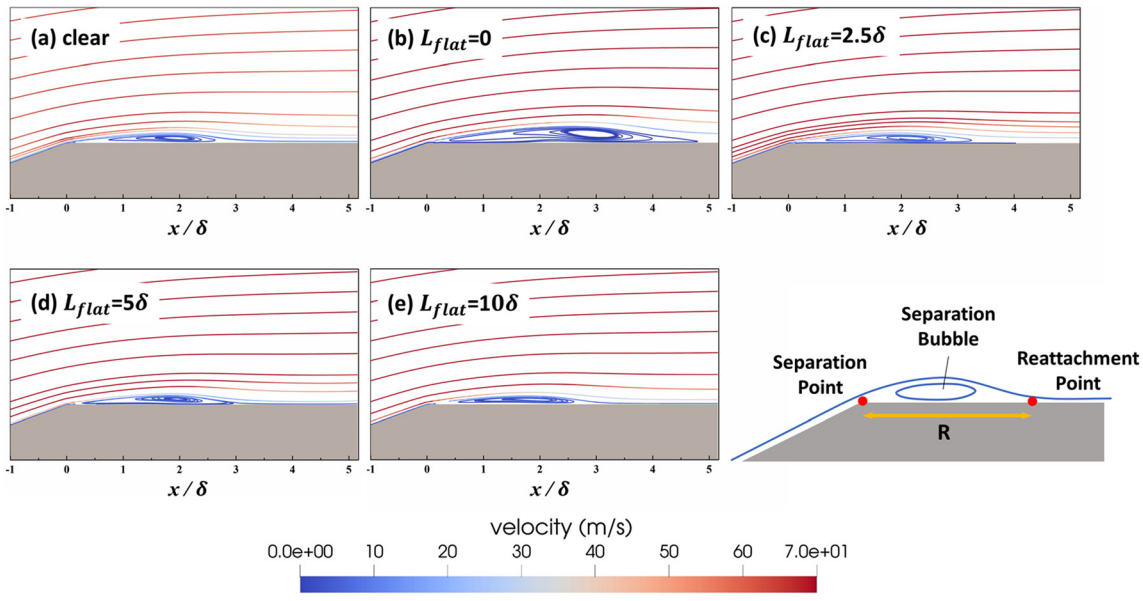

FIG. 17. The time-averaged streamlines colored with velocity values at the midplane for (a) the case without riblet, (b) the case with L_{flat} of 0, (c) the case with L_{flat} of 2.5δ, (d) the case with L_{flat} of 5δ, and (e) the case with L_{flat} of 10δ. In each case, the step angle is 20°.

and start wind tunnel tests on vehicle models. The application of riblets to reduce vehicle drag is a promising technology, but more research is needed.

ACKNOWLEDGMENTS

This research was funded by the China National Railway Group Science and Technology Program grant (No. K2023J047) and the CAS Project for Young Scientists in Basic Research (grant YSBR-045). The numerical calculations in this study were carried out on the ORISE Supercomputer.

AUTHOR DECLARATIONS

Conflict of Interest

The authors have no conflicts to disclose.

Author Contributions

Yeteng Wang: Conceptualization (lead); Data curation (lead); Formal analysis (equal); Funding acquisition (equal); Investigation (equal); Methodology (equal); Project administration (equal); Resources (equal); Validation (equal); Visualization (equal); Writing – original draft (lead); Writing – review & editing (equal). **Zhenxu Sun:** Conceptualization (equal); Formal analysis (equal); Funding acquisition (lead); Investigation (equal); Methodology (equal); Project administration (lead); Supervision (lead); Validation (equal); Writing – review & editing (equal). **Shengjun Ju:** Conceptualization (equal); Formal analysis (equal); Investigation (equal); Methodology (equal); Supervision (equal); Validation (equal). **Dilong Guo:** Conceptualization (equal); Funding acquisition (equal); Methodology (equal); Project administration (equal); Supervision (equal). **Bo Yin:** Conceptualization (equal); Investigation (equal); Methodology (equal). **Boyu Pan:** Conceptualization (equal); Formal analysis (equal); Investigation (equal); Validation (equal). **Kaiwei Nan:** Conceptualization (equal); Formal analysis (equal); Investigation (equal). **Guowei Yang:** Conceptualization (supporting); Funding acquisition (equal); Methodology (supporting); Project administration (equal); Supervision (supporting).

DATA AVAILABILITY

The data that support the findings of this study are available from the corresponding author upon reasonable request.

REFERENCES

Akbarzadeh, A. M. and Borazjani, I., "Reducing flow separation of an inclined plate via travelling waves," J. Fluid Mech. **880**, 831–863 (2019).
Bechert, D. W., Bruse, M., Hage, W., var der Hoeven, J. G. T., and Hoppe, G., "Experiments on drag-reducing surfaces and their optimization with an adjustable geometry," J. Fluid Mech. **338**, 59–87 (1997).
Ben-Nasr, O., Hadjadj, A., Chaudhuri, A., and Shadloo, M. S., "Assessment of subgrid-scale modeling for large-eddy simulation of a spatially-evolving compressible turbulent boundary layer," Comput. Fluids **151**, 144–158 (2017).
Boomsma, A. and Sotiropoulos, F., "Riblet drag reduction in mild adverse pressure gradients: A numerical investigation," Int. J. Heat Fluid Flow **56**, 251–260 (2015).
Choi, H., Moin, P., and Kim, J., "Direct numerical simulation of turbulent flow over riblets," J. Fluid Mech. **255**(1), 503 (1993).
Choi, H., Park, H., Sagong, W., and Lee, S., "Biomimetic flow control based on morphological features of living creatures," Phys. Fluids **24**(12), 121302 (2012).
Choi, K.-S., "Effects of longitudinal pressure gradients on turbulent drag reduction with riblets," in *Turbulence Control by Passive Means*, edited by E. Coustols (Springer, Netherlands, 1990), pp. 109–121.
Darwish, M. S. and Moukalled, F. H., "Normalized variable and space formulation methodology for high-resolution schemes," Numer. Heat Transfer, Part B **26**(1), 79–96 (1994).
Debisschop, J. R. and Nieuwstadt, F. T. M., "Turbulent boundary layer in an adverse pressure gradient—Effectiveness of riblets," AIAA J. **34**(5), 932–937 (1996).
El-Samni, O. A., Chun, H. H., and Yoon, H. S., "Drag reduction of turbulent flow over thin rectangular riblets," Int. J. Eng. Sci. **45**(2), 436–454 (2007).
García-Mayoral, R. and Jiménez, J., "Drag reduction by riblets," Philos. Trans. R. Soc., A **369**(1940), 1412–1427 (2011).
Goldstein, D., Handler, R., and Sirovich, L., "Direct numerical simulation of turbulent flow over a modeled riblet covered surface," J. Fluid Mech. **302**, 333–376 (1995).
Jee, S., Joo, J., and Medic, G., "Large-eddy simulation of a high-pressure turbine vane with inlet turbulence," in ASME Turbo Expo: Turbomachinery Technical Conference and Exposition, 2016.
Jelly, T. O., Jung, S. Y., and Zaki, T. A., "Turbulence and skin friction modification in channel flow with streamwise-aligned superhydrophobic surface texture," Phys. Fluids **26**(9), 095102 (2014).
Jiménez, J. and Moin, P., "The minimal flow unit in near-wall turbulence," J. Fluid Mech. **225**, 213–240 (1991).
Klumpp, S., Guldner, T., Meinke, M., and Schröder, W., "Riblets in a turbulent adverse-pressure gradient boundary layer," AIAA Paper No. AIAA 2010-4706, 2010.
Kurita, M., Nishizawa, A., Kwak, D., Iijima, H., Iijima, Y., Takahashi, H., Sasamori, M., Abe, H., Koga, S., and Nakakita, K., "Flight test of a paint-riblet for reducing skin-friction," in *Applied Aerodynamics Conference* (American Institute of Aeronautics and Astronautics, 2018).
Lee, S.-J. and Lee, S.-H., "Flow field analysis of a turbulent boundary layer over a riblet surface," Exp. Fluids **30**(2), 153–166 (2001).
Luchini, P., Manzo, F., and Pozzi, A., "Resistance of a grooved surface to parallel flow and cross-flow," J. Fluid Mech. **228**, 87–109 (1991).
Medic, G., Zhang, V., Wang, G., Joo, J., and Sharma, O. P., "Prediction of transition and losses in compressor cascades using large-eddy simulation," J. Turbomach. **138**(12), 121001 (2016).
Mueller, T. J. and DeLaurier, J. D., "Aerodynamics of small vehicles," Annu. Rev. Fluid Mech. **35**, 89–111 (2003).
Nicoud, F. and Ducros, F., "Subgrid-scale stress modelling based on the square of the velocity gradient tensor," Flow, Turbul. Combust. **62**(3), 183–200 (1999).
Qin, S., Koochesfahani, M., and Jaberi, F., "Large eddy simulations of unsteady flows over a stationary airfoil," Comput. Fluids **161**, 155–170 (2018).
Raayai-Ardakani, S. and McKinley, G. H., "Geometric optimization of riblet-textured surfaces for drag reduction in laminar boundary layer flows," Phys. Fluids **31**(5), 053601 (2019).
Temmerman, L., Leschziner, M. A., Mellen, C. P., and Fröhlich, J., "Investigation of wall-function approximations and subgrid-scale models in large eddy simulation of separated flow in a channel with streamwise periodic constrictions," Int. J. Heat Fluid Flow **24**(2), 157–180 (2003).
Truong, T. V. and Pulvin, P., "Influence of wall riblets on diffuser flow," Appl. Sci. Res. **46**(3), 217–227 (1989).
Viswanath, P. R., "Aircraft viscous drag reduction using riblets," Prog. Aerosp. Sci. **38**(6–7), 571–600 (2002).
Wallace, J. M., "Quadrant analysis in turbulence research: History and evolution," Annu. Rev. Fluid Mech. **48**(1), 131–158 (2016).
Walsh, M., "Turbulent boundary layer drag reduction using riblets," AIAA Paper No. AIAA 1982-169, 1982.
Weickert, M., Teike, G., Schmidt, O., and Sommerfeld, M., "Investigation of the LES WALE turbulence model within the lattice Boltzmann framework," Comput. Math. Appl. **59**(7), 2200–2214 (2010).
Zhang, Y., Chen, H., Fu, S., and Dong, W., "Numerical study of an airfoil with riblets installed based on large eddy simulation," Aerosp. Sci. Technol. **78**, 661–670 (2018).